nature nanotechnology

Article

https://doi.org/10.1038/s41565-023-01323-4

Machine-learning-assisted single-vessel analysis of nanoparticle permeability in tumour vasculatures

Received: 5 July 2022

Accepted: 6 January 2023

Mingsheng Zhu[1,7], Jie Zhuang[2,7], Zhe Li[3,4], Qiqi Liu[1], Rongping Zhao[2], Zhanxia Gao[2], Adam C. Midgley[1], Tianyi Qi[1], Jingwei Tian[1], Zhixuan Zhang[1], Deling Kong[1], Jie Tian[4]✉, Xiyun Yan[5,6]✉ & Xinglu Huang[1]✉

The central dogma that nanoparticle delivery to tumours requires enhanced leakiness of vasculatures is a topic of debate. To address this, we propose a single-vessel quantitative analysis method by taking advantage of protein-based nanoprobes and image-segmentation-based machine learning (nano-ISML). Using nano-ISML, >67,000 individual blood vessels from 32 tumour models were quantified, revealing highly heterogenous vascular permeability of protein-based nanoparticles. There was a >13-fold difference in the percentage of high-permeability vessels in different tumours and >100-fold penetration ability in vessels with the highest permeability compared with vessels with the lowest permeability. Our data suggest passive extravasation and transendothelial transport were the dominant mechanisms for high- and low-permeability tumour vessels, respectively. To exemplify the nano-ISML-assisted rational design of nanomedicines, genetically tailored protein nanoparticles with improved transendothelial transport in low-permeability tumours were developed. Our study delineates the heterogeneity of tumour vascular permeability and defines a direction for the rational design of next-generation anticancer nanomedicines.

Transport across endothelial cells is an essential process for boosting the delivery efficiency of anticancer agents[1–3]. The endothelial cells of tumour blood vessels contain gaps between endothelial cells (for example, interendothelial gaps) and transcellular fenestrae (for example, vesiculo-vacuolar organelles (VVOs))[4–6]. On the basis of this vessel leakiness, an enhanced penetration and retention mechanism was proposed in 1986 (ref. [7]), and has been considered a central principle for the development of tumour-targeting nanocarriers. A recent study demonstrated that up to 97% of nanoparticles enter tumours through an active transendothelial transport mechanism as opposed to via passive extravasation[8]. This conclusion was controversial in the community, but did provide a 'wake-up call' to shift research towards delineating the heterogeneity of the mechanisms of vascular permeability. However, the current lack of available quantitative strategies has hampered progress in understanding the vascular permeability of nanoparticles. Quantitative analysis of individual blood vessels makes it possible to determine

---

[1] Key Laboratory of Bioactive Materials for the Ministry of Education, College of Life Sciences, State Key Laboratory of Medicinal Chemical Biology, and Frontiers Science Center for Cell Responses, Nankai University, Tianjin, China. [2] School of Medicine, Nankai University, Tianjin, China. [3] School of Cyberspace Science and Technology, University of Science and Technology of China, Hefei, China. [4] CAS Key Laboratory of Molecular Imaging, State Key Laboratory of Management and Control for Complex Systems, Institute of Automation, Beijing, China. [5] CAS Engineering Laboratory for Nanozymes, Institute of Biophysics, Chinese Academy of Sciences, Beijing, China. [6] University of Chinese Academy of Sciences, Beijing, China. [7] These authors contributed equally: Mingsheng Zhu, Jie Zhuang. ✉e-mail: tian@ieee.org; yanxy@ibp.ac.cn; huangxinglu@nankai.edu.cn

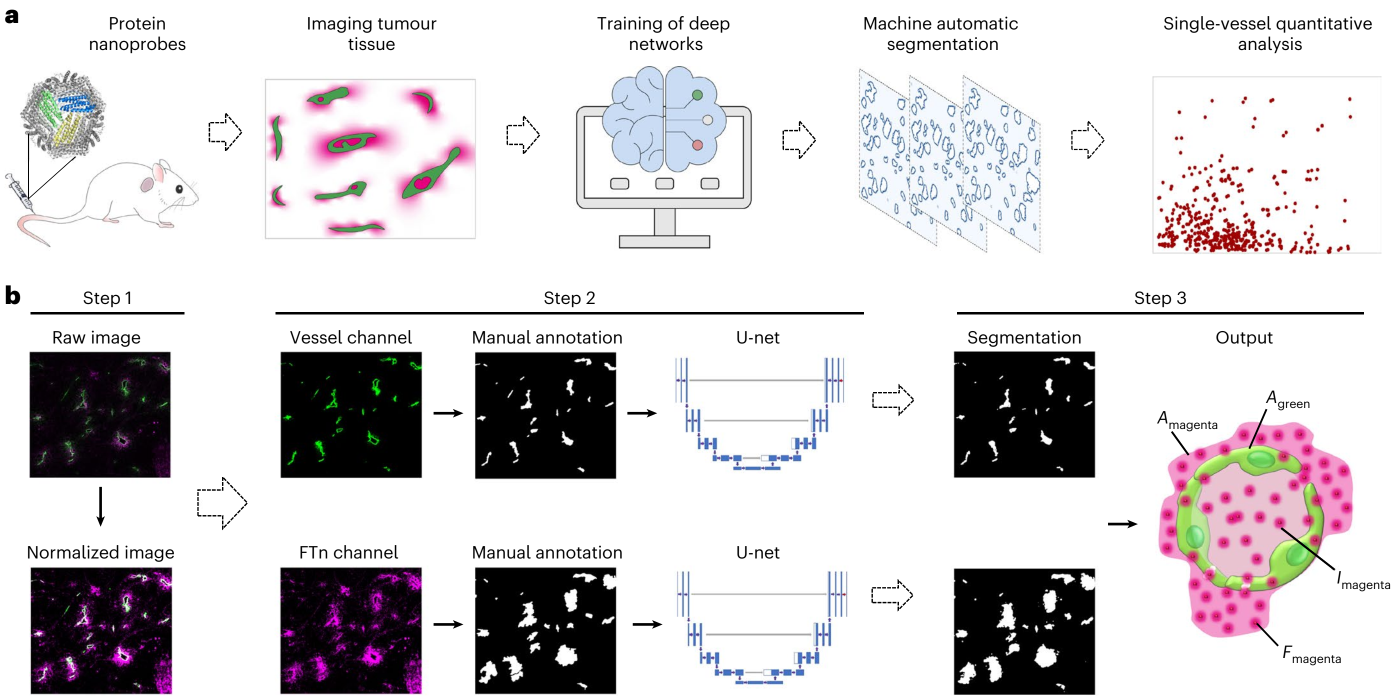

Fig. 1 | ML-based single-vessel analysis method. a, This approach includes multiple steps. First, the images containing spatial distribution of vessel and protein nanoprobes were acquired following systemic administration via the tail vein of tumour-bearing mice. Next, manually annotated images were trained using a deep neural network. The collected images from various tumour tissues were automatically segmented using the trained models. Finally, the features of input images were automatically segmented and quantitatively analysed. **b**, A detailed workflow for ML-based automatic image segmentation and quantitative analysis. During step 1, the images of tumour tissues were preprocessed. During step 2, two-channel images including vessel channel and nanoprobe channel were separated and their boundaries were manually annotated. The ML-based models were established by training of manually annotated images using the U-net convolutional neural network. During step 3, using the established image segmentation models, a large number of collected images were input for machine automatic segmentation. The quantification information was also automatically output in terms of manually setting indices.

the extent of vascular permeability, but is a time-consuming, laborious and resource-intensive task. Machine learning (ML) can be employed to rapidly analyse big data, and identify trends and patterns not obvious to human operators[9–12]. Inspired by the advantages of ML, we sought to fill the knowledge gap in high-throughput quantification of vascular permeability by devising a single-vessel analysis approach on the basis of protein-based nanoprobes and image-segmentation-based ML technology (nano-ISML). Using nano-ISML, we aimed to answer three key questions on nanoparticle delivery to tumours: (1) Is the vascular permeability in different tumours and blood vessels heterogeneous, and if so, how can differential tumour permeability be quantifiably classified? (2) What is the potential mechanism of permeability in different vessels? (3) Does our approach make it possible to modulate the changes in vascular permeability, thereby guiding the development of personalized delivery strategies?

Single-vessel analysis of vascular permeability

To perform quantitative analysis of vascular permeability, we originated a single-vessel analysis approach by combining the vascular permeability of fluorescent-dye-labelled protein nanoprobes with the advantages gained from ML in image segmentation. The workflow is shown in Fig. 1a. Genetically recombinant human ferritin nanocages (FTn) were chosen as model nanoparticles because they possess reproducible and homogeneous size (that is, 12 nm) and structure[13,14], and can be visualized after dye labelling (Supplementary Fig. 1a). To understand the in vivo dynamic behaviours of FTn, we first administered Cy5.5-labelled FTn to tumour-bearing mice for in vivo imaging. A burst accumulation of FTn was observed in tumours, and reached a maximum accumulation at 30 min postadministration (Supplementary Fig. 1b). Deep learning has been widely utilized in automatic image segmentation[15–17]. To quantitatively analyse the vascular permeability of the images obtained from tumour tissue, we next developed an ML-based model (Fig. 1b); the detailed procedures are described in the Methods. Using this model, the boundaries of blood vessel profiles and FTn coverage areas were automatically segmented from the input images, followed by the extraction of parameters derived from vessels and FTn penetration. We provide example images, including the original microscopy image (confocal), manual annotation (that is, gold-standard labels), and machine segmentation images (prediction) (Supplementary Fig. 2a). Following the above workflow, the models were trained using the input images randomly extracted from different tumour model types. The established two models (that is, vessel and FTn penetration) showed ~90 and ~80% accuracy in blood vessel and FTn penetration across 32 tumour models, respectively (Supplementary Fig. 2b). By inter-annotation analysis[18], the accuracies of manual annotations were comparable with that of the predicted segmentation (Supplementary Table 1).

Next, we sought to evaluate the permeability of individual vessels in various tumour models using nano-ISML. The images collected from various tumour types were obtained 30 min after administration of Cy5-labelled FTn (Supplementary Fig. 2c). Based on automatic machine segmentation of the images, we extracted the total FTn coverage area for each vessel (A_{magenta}), the coverage area of each vessel (A_{green}), the total Cy5 fluorescence intensity for each vessel (F_{magenta}) and the Cy5 fluorescence intensity in each vessel lumen (I_{magenta}) (Supplementary Fig. 2d). Based on the above four features, we defined a series of indices for single-vessel quantitative analysis to include three aspects: blood

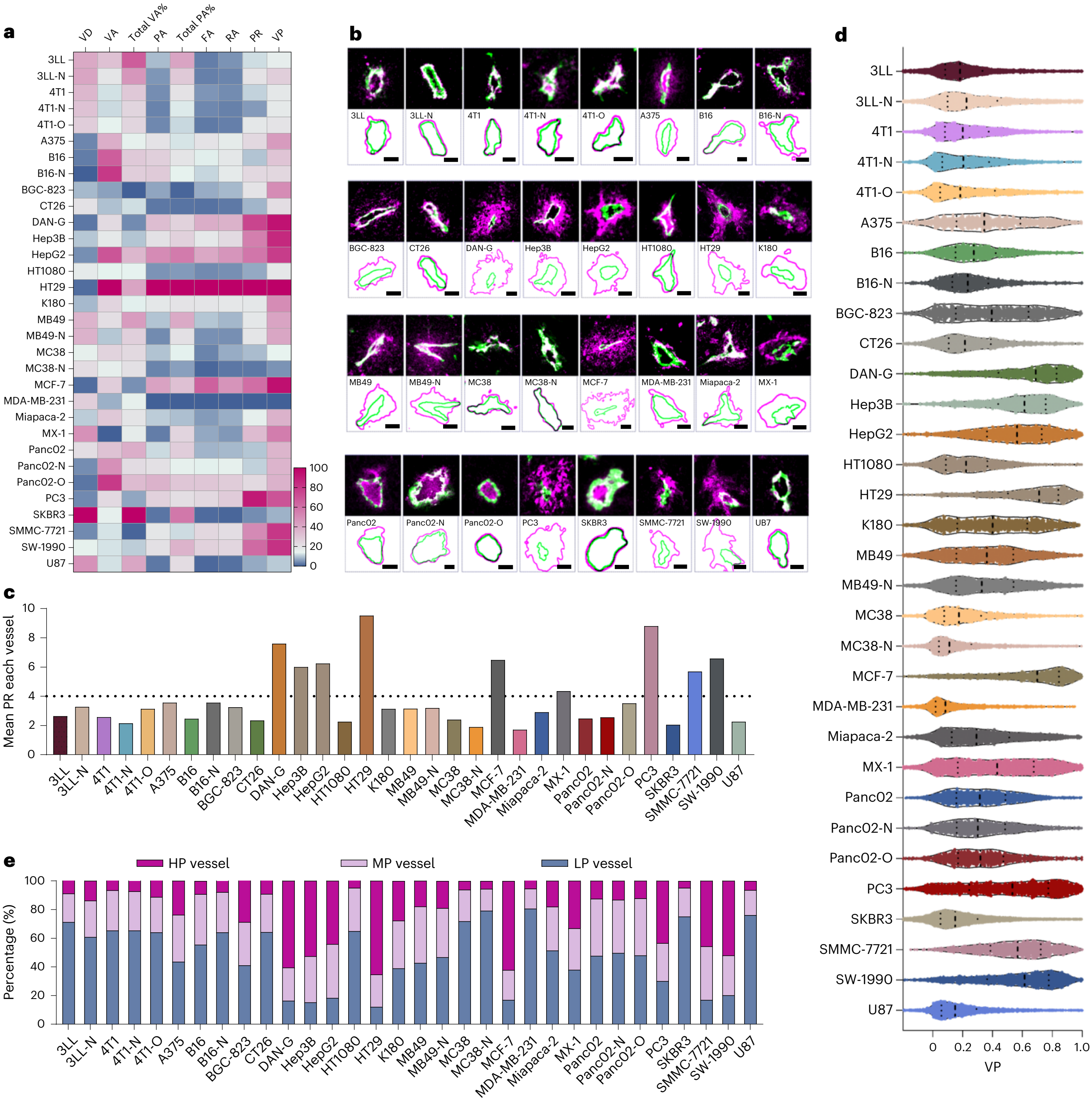

Fig. 2 | Quantitative analysis of heterogeneous vascular permeability using the nano-ISML method. a, Heatmap showing the penetration patterns of blood vessels for 32 tumour models with rows corresponding to tumour models and columns corresponding to vessels and FTn penetration ($n = 4$–5 tumours for each tumour type). The colour scale shows the normalized values by normalizing the maximum value for each parameter as 100. **b**, Representative vessels of FTn away from vessels for 32 tumour models. For each tumour model, the mean PR of each single vessel was extracted. Upper: confocal image for vessel (green) and FTn penetration (magenta); lower: the overlay outline of vessel and FTn penetration based on the predicted image from the ML-based model. Scale bar, 20 µm. **c**, Mean PR for each vessel in various tumour models. Tumours were manually divided into HP tumours and LP tumours based on a PR cut-off value of 4, as indicated by the dashed line. **d**, Violin plot analysis of the heterogeneous distribution of VP for each vessel in 32 tumour models. Each dot represents the VP value of a single vessel, and at least 1,000 vessels were analysed for each tumour model. **e**, All vessels for each tumour model were manually divided into three permeability types according to their VP values: HP (>0.6, ≤1), MP (≥0.3, ≤0.6) and LP (<0.3). The percentages of the three permeability types in all vessels were calculated based on these cut-off values.

vessels, FTn penetration, and the correlation between vessels and FTn penetration (vessel-FTn) (Supplementary Table 2). To determine the hidden features of the images, we collected and analysed sufficiently large numbers of vessels, with at least 1,000 vessels per tumour and a total of 67,530 vessels analysed in 32 tumours (Supplementary Fig. 3a). Nine important indices were preferentially and individually analysed for each vessel assessed, including vessel area (VA), FTn penetration area (PA), FTn penetration amount (FA), FTn penetration area ratio (PR) and vascular permeability (VP). We first compared the feature analysis extracted from manual annotation and machine segmentation, and the results revealed that the segmented images obtained from machine models were highly similar to those of manual annotations (Supplementary Fig. 3b). Subsequently, the nine indices were normalized and displayed as heatmap images, and the results of vessel, FTn and vessel-FTn indices demonstrated that blood vessel permeability across different tumour model types was highly heterogeneous (Fig. 2a). The detailed quantitative analysis is listed in the Supplementary Fig. 4 and Supplementary Table 3.

To better understand the heterogeneity in vascular permeability, PR and VP were chosen as indices for further data mining. We used nano-ISML to quantify the mean PR of blood vessels in various tumours. The representative individual vessels and their corresponding FTn penetrations are shown in terms of the length-scale-dependent geometric segmentation area (Fig. 2b). For example, at a length scale of 20 µm, the blood vessels in HT29 and HepG2 tumours showed a large area of permeability, whereas poor penetration was observed in 3LL and SKBR3 tumours. Quantitative analysis of all vessels in 32 tumours demonstrated that the mean PR ranged from 1.70 to 9.52 (Fig. 2c) and the highest vessel PR was >100-fold greater than the lowest vessel PR (Supplementary Fig. 4c). We thus divided tumours into two categories by scoring tumour permeability, using a cut-off PR value of 4, thereby grouping tumours into high-permeability (HP) and low-permeability (LP) categories. The results indicated that DAN-G, Hep3B, HepG2, HT29, MCF-7, MX-1, PC3, SMMC-7721 and SW-1990 were HP tumours, whereas other tumours showed low permeability. To further elucidate the penetration ability of individual vessels, violin plot analyses were performed to visualize the distribution of the VP values. As shown in Fig. 2d, a highly heterogeneous distribution of VP was observed for the blood vessels of each tumour, indicating that vascular permeability was highly heterogeneous for different vessels within the same tumour type. Moreover, the distribution of the dominant vessel population varied greatly among different tumour model types. Based on the violin plot analyses of VP distribution, we classified blood vessels of each tumour into three permeability types, according to their VP values: LP vessels (<0.3), medium- permeability (MP) vessels (0.3–0.6) and HP vessels (>0.6). The percentage distributions of the three kinds of vessels in each tumour are displayed in Fig. 2e. The HP vessels of HT29 account for 65.3% of all vessels but comprised only 12.0% of LP vessels. In contrast, there were 4.9 and 8.7% HP vessels observed in SKBR3 and 3LL, respectively. These quantitative analyses revealed that the VP was dependent on tumour type and was a result of heterogeneous susceptibility to penetration exhibited by different vessels. Additionally, sequential tissue sectioning of three permeable tumours revealed that the VP values of tumours was not significantly affected by different tissue layers with defined tissue section thickness (Supplementary Fig. 5).

Heterogeneous penetration mechanism of tumour vessels

To explore the penetration mechanism of tumour vessels, we used a Zombie model[8] to assess the penetration of FTn, allowing us to estimate the extent of the contribution of passive extravasation and active transendothelial transport. Using nano-ISML, HT29 and 3LL tumours (HP and LP tumours, respectively) were chosen to analyse FTn penetration in Zombie models and control tumour-bearing mice. Confocal images and violin plot analyses revealed that the vascular permeability of FTn in control HT29 tumours was consistent with Zombie HT29 tumours (Fig. 3a). However, compared with control 3LL tumours, a significant reduction in permeability was observed in Zombie 3LL tumours. The results implied that the FTn penetration in HP tumours and HP vessels was mainly dependent on passive extravasation mechanisms, whereas active transendothelial transport played a leading role in LP tumours.

To further explore permeability mechanisms, we generated iron oxide nanoparticles (IO) in the hollow cavity of FTn (FTn-IO) via a biomimetic synthesis approach[19] (Supplementary Fig. 6a). Transmission emission microscopy (TEM) images of tumour tissues at 30 min showed that the individual FTn-IO were directly visualized in the vessel lumens, endothelial lining and extravascular space (Supplementary Fig. 6b). We next evaluated how FTn-IO was transported from the vascular lumen to the extravascular space. Two mechanisms were identified in this process: passive extravasation and active transendothelial transport. From TEM observations of 73 blood vessels, we observed two passive extravasation mechanisms that participated in direct diffusion of FTn-IO from the lumen to the extravascular space, mainly via interendothelial gaps (Supplementary Fig. 6c) and VVOs (Supplementary Fig. 6d). The sizes of the interendothelial gaps were not uniform, and reached a maximum size of >600 nm in our observations. VVOs, which are grape-like clusters of interconnected vesicles, are pathways of direct connection between the lumen and the extravascular space and are often found in tumour microvasculature[20,21]. Additionally, tight junctions with small gaps (~10 nm) were typically found between endothelial cell–endothelial cell junctions, but we did not observe extravasated FTn-IO (Supplementary Fig. 6e). To further determine the active transport processes involved, we first explored active capture–uptake mechanisms in 3LL tumours. Three main capture–uptake mechanisms were observed by TEM: pinocytosis, phagocytosis and receptor-mediated endocytosis (Fig. 3b). We determined that pinocytosis was the principal capture–uptake mechanism for FTn-IO by counting the number of FTn-IO. In typical endothelial cells, pinocytosis, phagocytosis and receptor-mediated endocytosis of FTn-IO accounted for 82.9 ± 2.6%, 14.8 ± 2.2% and 2.3 ± 0.5%, respectively (Fig. 3c). To verify the role of pinocytosis, 3LL tumours were pretreated with a pinocytosis inhibitor, 5-(*N*-ethyl-*N*-isopropyl) amiloride (EIPA), followed by FTn administration. Confocal images and single-vessel quantitative analysis demonstrated that the permeability of the vessels was decreased after treatment with EIPA (Fig. 3d,e), implying that pinocytosis played a

Fig. 3 | Heterogeneity of vascular permeability mechanism. a, Zombie model with HT29 and 3LL demonstrates active or passive pathways for FTn penetration. Left: representative confocal images for vascular penetration in control and Zombie mice. Scale bar, 50 µm. Right: violin plot analysis of VP distribution using the nano-ISML approach. **b**, TEM images of active capture mechanisms of endothelial cells. Representative images of the entire vessel (left; scale bar, 1 µm) and enlarged images (right; scale bar, 100 nm) of three typical capture mechanisms (that is, pinocytosis, phagocytosis and endocytosis). L and R represent lumen of endothelial cell and red blood cell, respectively. Black triangles indicate the FTn-IO in the enlarged images. **c**, Quantitative analysis of the contribution of three capture mechanisms for the active pathway by counting FTn-IO numbers observed in tumour blood vessels. Each dot represents single vessel, and total 32 vessels were analysed. **d**, Single-vessel analysis of 3LL tumours with or without the pinocytosis inhibitor EIPA (3LL-EIPA). Representation confocal images of tissue sections from 3LL and 3LL-EIPA are shown (left). Blue, nucleus; green, vessel; magenta, FTn. Scale bar, 50 µm. Violin plot analysis of the distribution of VP for each vessel is listed (right). **e**, Quantitative analysis of the percentage of HP, MP and LP vessels, obtained from **d**. **f**, Typical features of formed vesicles (black star) in active vessels and inactive vessels. Representative TEM images of formed large vesicles for active vessel (top left) and small vesicles for inactive vessel (bottom left). Scale bar, 100 nm. Quantitative analysis of the distribution of vesicle diameters in active vessels (top right, $n = 4,850$) and inactive vessels (bottom right, $n = 1,560$). **g**, Diagram illustrating the dominant vascular penetration mechanism in HP tumours and LP tumours. HP tumours are primarily dependent on the passive extravasation mechanism via interendothelial gap and VVO pathways, whereas active transendothelial transport mechanism following pinocytosis is the dominant manner for LP tumours. Data are presented as mean ± s.e.m.

critical role in vascular penetration of nanoparticles. After capture by endothelial cells, the protruded 'arms' of the endothelial lining connect to form vesicles that are translocated into extravascular space via exocytosis. From TEM observations, we determined that the diameter of the formed vesicles was highly heterogeneous in different vessels (Supplementary Fig. 6f,g). The vesicles reached microscale in size

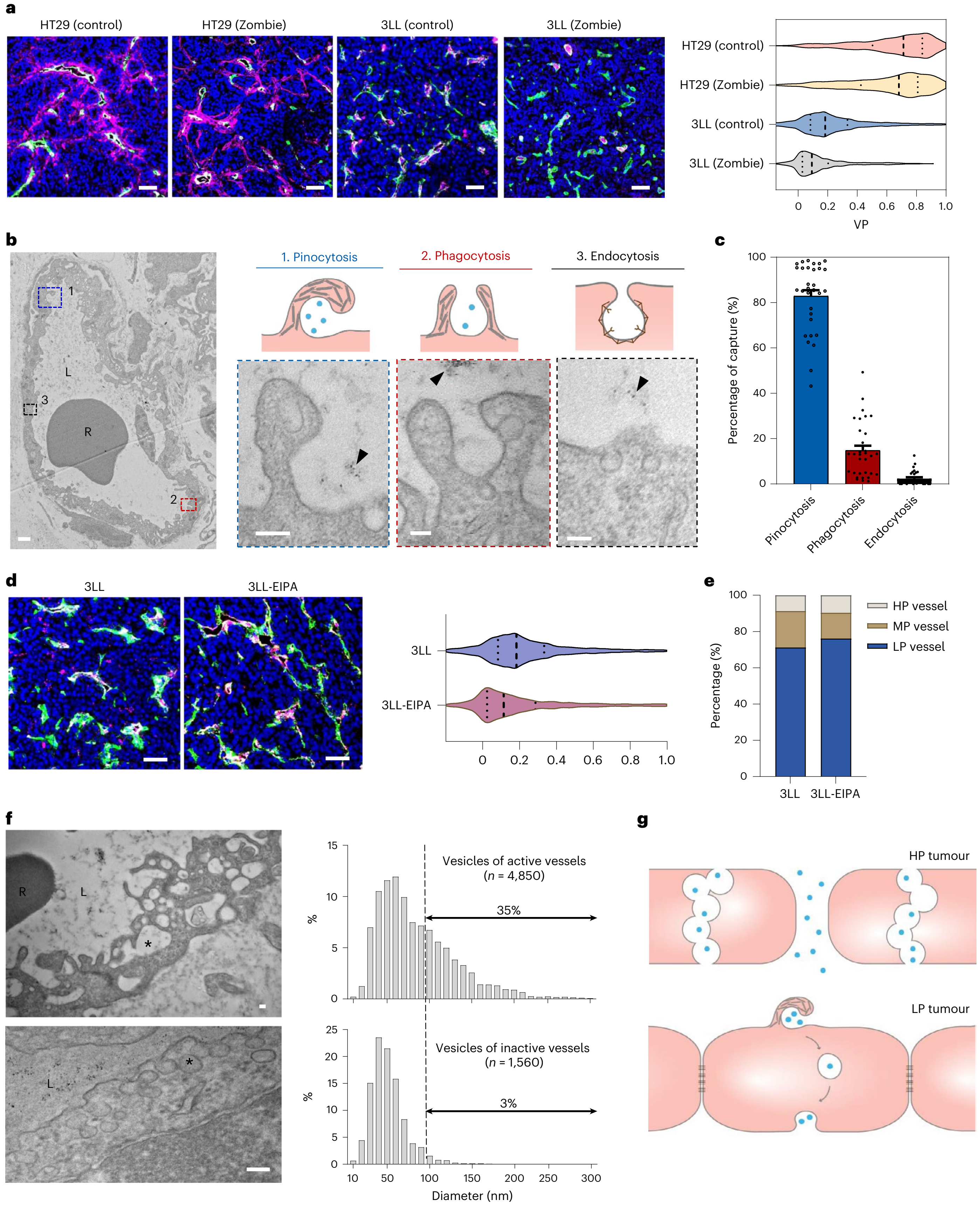

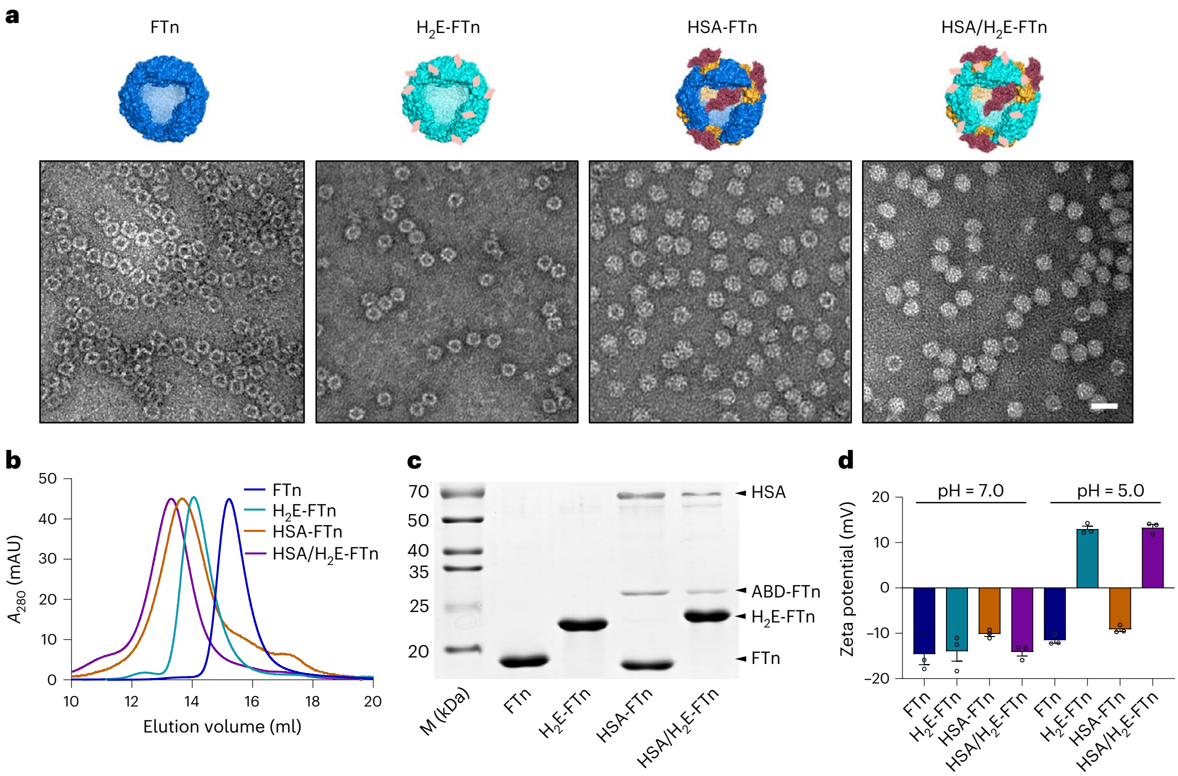

Fig. 4 | Characterization of FTn and FTn variants. a, Diagrammatic representations and corresponding TEM images of FTn and its variants. The $(H_2E)_9$ fragments (pink) were directly incorporated into FTn subunits. Prior to HSA binding (red), an ABD fragment (orange) was genetically incorporated into the FTn subunit, followed by self-assembly with the FTn subunit. For HSA/H_2E-FTn, FTn subunits containing H_2E or ABD fragments were self-assembled into a single particle, which was further bound with HSA. Scale bar, 20 nm. **b**, Size-exclusion chromatography analysis of the sizes of FTn and its variants in a protein purification equipment. A_{280}, absorbance at 280 nm; mAU, milli absorbance unit. **c**, SDS–PAGE analysis of the resulting FTn and its variants. **d**, Zeta potential of FTn and its variants at pH 7.0 and pH 5.0. $n = 3$ independent experiments. Data are presented as mean ± s.e.m.

for the active vessels but were <100 nm in inactive vessels (Fig. 3f, left). Quantitative analysis found that the vesicles >100 nm in active and inactive vessels accounted for approximately 35 and 3%, respectively (Fig. 3f, right). Active transport processes, including capture, vesicle formation, transport and exocytosis, were clearly observable (Supplementary Fig. 6h,i). Based on these results, we proposed heterogeneous potential mechanisms of nanoparticle transport across tumour blood vessels (Fig. 3g). For HP tumours, passive extravasation via interendothelial gaps and VVOs was the predominant penetration mechanism. In addition to a small number of high-permeability vessels, nanoparticle transport to the extravascular space by the vessels in LP tumours was predominantly dependent on active transendothelial transport mechanisms following active capture of nanoparticles, mainly by pinocytosis by active vessel endothelial cells.

Preparation and characterization of FTn variants

Modulating the vascular permeability of nanoparticles offers an effective approach to facilitating the enhanced efficacy of drug delivery. We thus sought to explore how to improve the vascular permeability of FTn in LP tumours. We found that FTn localized in lysosomes, and subsequently remained trapped in lysosomes following uptake by human umbilical vein endothelial cells (HUVECs) (Supplementary Fig. 7a). Lysosomes are important organelles for inducing intracellular degradation of exogenous particles[22,23]. Thus, we hypothesized that reducing lysosome trapping to improve transport efficacy of endothelial cells would be an efficient strategy for boosting the vascular permeability of FTn. Following this line of thought, we developed three FTn variants based on genetic engineering strategies: $(H_2E)_9$-fused FTn (H_2E-FTn), human serum albumin (HSA)-bound FTn (HSA-FTn) and HSA-bound H_2E-FTn (HSA/H_2E-FTn). The endosomolytic $(H_2E)_n$ peptide is capable of proton buffering to aid endosomolysis[24] and HSA is preferentially trafficked to the Golgi apparatus[25–27] followed by secretion of exocytic vesicles and exocytosis. Details of the FTn variants are described in the Methods. TEM images showed the structure of FTn and its variants after negative staining (Fig. 4a). Size-exclusion chromatography analysis indicated that the FTn variants were of larger molecular sizes than FTn (Fig. 4b), and this was further confirmed by dynamic light scattering (DLS) analysis (Supplementary Fig. 7b). Importantly, the expected nanostructures with genetic incorporation and/or HSA binding were confirmed by SDS–polyacrylamide gel electrophoresis (SDS–PAGE) characterization (Fig. 4c). The zeta potential changes of H_2E and HSA/H_2E-FTn between pH 7.0 and pH 5.0 demonstrated the protonation effect of H_2E in mediating the switching of FTn-based nanoparticles to positive charge in acidic microenvironments (Fig. 4d). Further DLS analysis revealed that the protein particles remained stable at pH 5.0 (Supplementary Fig. 7c). Cell viability assays confirmed that FTn and its various nanocarriers did not induce significant cytotoxicity (Supplementary Fig. 7d).

Improved vascular permeability in LP tumours

Next, we sought to explore whether the tailored FTn variants improved the transport efficacy of endothelial cells. First, we studied the intracellular fate of FTn and its variants, including cell uptake, intracellular trafficking and exocytosis. Confocal images showed efficient cell uptake of FTn and its variants after incubation with HUVECs (Fig. 5a). Unlike the exclusive distribution of FTn in lysosomes, the FTn variants

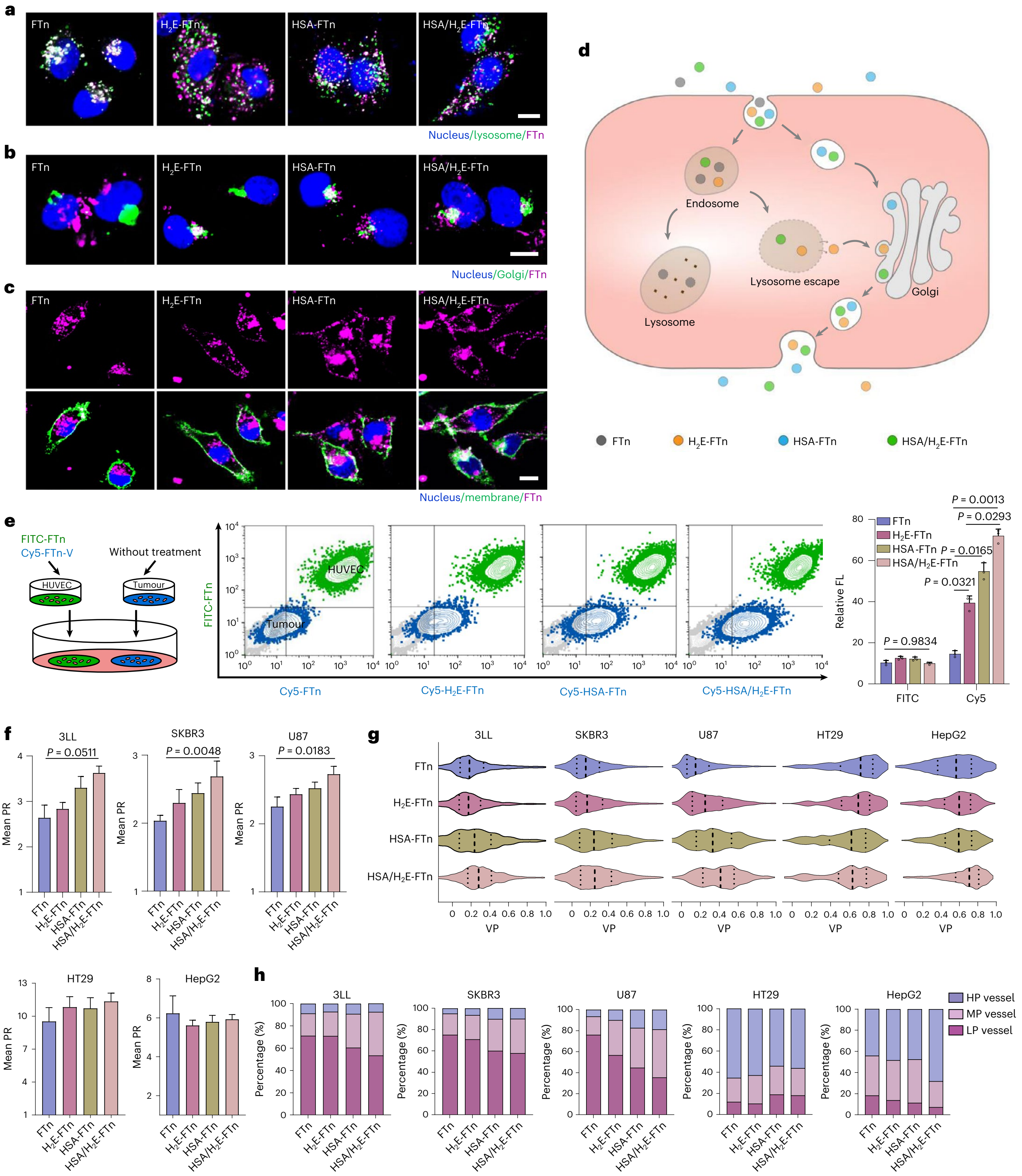

partly localized into lysosomes after uptake. Furthermore, we found that H_2E-FTn, HSA-FTn and HSA/H_2E-FTn co-localized with the Golgi, whereas the distribution of FTn was negligible in the Golgi (Fig. 5b). By culturing for another 6 h after uptake, exocytosis of FTn variants was clearly higher than that of FTn (Fig. 5c). Quantitative analysis further verified the enhanced transport efficacy of FTn variants (Supplementary Fig. 7e). Based on the role of the Golgi in exocytosis[28,29] and the above results, the potential intracellular fate of FTn and its variants was summarized and is shown in Fig. 5d. We further investigated whether FTn variants improve translocation of FTn from endothelial cells to tumour cells, as a result of the enhanced exocytosis by the Golgi. Flow cytometry analysis revealed the synergistic role of

Fig. 5 | Enhancement of active transendothelial transport. a–**c**, Confocal images of HUVECs demonstrating co-localization (white) of FTn and FTn variants (magenta) with lysosomes (**a**, green), Golgi (**b**, green) and membrane (**c**, green). Scale bar, 5 μm. **d**, Schematic illustration showing a transcytosis-enhanced strategy of endothelial cells by boosting the Golgi-dependent exocytosis pathway. After uptake, FTn are easily trapped into lysosomes and are further degraded. For H_2E incorporation, the particles are capable of escaping from lysosomes, followed by exocytosis via a Golgi-dependent pathway. The HSA-binding particles directly travel into the Golgi for exocytosis. The exocytosis of HSA/H_2E-FTn is dependent on the two routes above. **e**, Flow cytometry analysis of the transcytosis mechanism by coincubation of HUVECs and tumour cells. The HUVECs seeded onto coverslip slides (green) were pretreated with FITC-labelled FTn and Cy5-labelled FTn variants (FTn-V) and the untreated tumour cells were seeded onto another coverslip slide (blue). The tumour cells with fluorescence signal (FITC and Cy5) were collected for quantitative analysis using flow cytometry. The gate was set to 'viable' cells in the FSC/SSC plot. $n = 3$ independent experiments. **f**, Mean PR of each blood vessel in various tumours after treatment with FTn and its variants for 30 min. 3LL, SKBR3, U87, $n > 900$ vessels each group; HT29, $n > 100$ vessels each group; HepG2, $n > 200$ vessels each group. **g**, Violin plot analysis of the distribution of VP for each vessel in different tumour models using the nano-ISML approach following administration of FTn and its variants for 30 min. **h**, Quantitative analysis of the percentage of HP, MP and LP vessels in different tumour-bearing mice treated with FTn and its variants, obtained from **g**. Data are presented as mean ± s.e.m. and statistical analysis was performed by one-way ANOVA with Tukey's post hoc test for comparison.

H_2E and HSA in the transcytosis of FTn (Fig. 5e). Using nano-ISML, we next quantitatively evaluated the vascular permeability of FTn and its variants in HP and LP tumours. The results demonstrated that the mean PR of HSA/H_2E-FTn for 3LL, U87 and SKBR3 were increased by 37, 21 and 32%, respectively, compared with that of FTn alone (Fig. 5f and Supplementary Fig. 8). In contrast, the mean PR for the vessels of HP tumours (that is, HT29, HepG2) showed no clear changes. Violin plot analysis confirmed the improved permeability of FTn variants in LP tumours (that is, 3LL, SKBR3, U87) compared with that of FTn (Fig. 5g). However, the changes in nanoparticle vascular permeability resulting from H_2E/HSA incorporation was limited in HP tumours due to the masking by the VP distribution population in HP vessels. Quantitative analysis revealed that FTn variants converted LP vessels into the indices that defined MP vessels in LP tumours (Fig. 5h). We also found that HSA/H_2E-FTn showed a greater conversion efficacy than H_2E-FTn and HSA-FTn, implying their synergistic effect on improving active transendothelial transport.

Enhancing vascular permeabiltiy boosts therapeutic outcomes

We next studied whether FTn variants could improve therapeutic outcomes by enhancing vascular permeability. In vivo behaviours were first compared following intravenous administration of FTn and its variants. We found that H_2E and/or HSA incorporation did not significantly affect the in vivo blood circulation time of FTn (Supplementary Fig. 9a). In vivo tumour accumulation and biodistribution of FTn and its variants was further investigated by imaging and monitoring of both LP and HP tumours. To do this, SKBR3 and HT29 were simultaneously inoculated into the left and right shoulders of the same mice, respectively (Fig. 6a). We observed obvious tumour accumulation of FTn and its variants in both LP and HP tumours, and greater accumulation was found in HP tumours compared with that in LP tumours. Quantitative analysis of the LP/HP ratio demonstrated that FTn variants resulted in an improved LP:HP ratio at 12 h compared with that of FTn. The elevated LP:HP ratio at 12 h was higher than the ratio observed at 1 h, especially for HSA/H_2E-FTn. These results suggested that the contribution of active transendothelial transport was in effect. Ex vivo imaging and quantitative analysis revealed that the biodistribution of FTn was comparable to its variants at 24 h after administration (Supplementary Fig. 9b). We next sought to evaluate whether FTn variants could result in improved in vivo antitumour efficacy. A chemotherapeutic drug, doxorubicin (Dox), was loaded into FTn and its variants (Supplementary Fig. 9c), following a previously described methodology[30]. Through measurements of total protein and Dox concentrations, the number of Dox molecules loaded into each FTn, H_2E-FTn, HSA-FTn and HSA/H_2E-FTn was determined to be 67.4 ± 5.6, 66.2 ± 3.7, 65.9 ± 4.3 and 59.8 ± 5.9, respectively. Confocal images revealed that the Dox-loaded FTn and FTn variants were successfully released after uptake and delivered to the nuclei of tumour cells (Supplementary Fig. 9d). Subsequently, Dox-loaded FTn (FTn-Dox), Dox-loaded H_2E-FTn (H_2E-FTn-Dox), Dox-loaded HSA-FTn (HSA-FTn-Dox) and Dox-loaded HSA/H_2E-FTn (HSA/H_2E-FTn-Dox) were intravenously injected into mice xenografted with LP tumours (that is, 3LL, SKBR3) and HP tumours (that is, HT29) every 3 days. As expected, systemically administered Dox-loaded FTn and FTn variants significantly delayed tumour growth, regardless of whether the tumours were LP or HP (Fig. 6b). Compared to H_2E-FTn-Dox and HSA-FTn-Dox, HSA/H_2E-FTn-Dox showed a synergistic therapeutic action in LP tumours, but this action was not observed in HP tumours. Survival was also effectively improved for LP-tumour-xenografted mice treated with HSA/H_2E-FTn-Dox, compared with H_2E-FTn-Dox and HSA-FTn-Dox. In contrast, HSA/H_2E-FTn-Dox did not significantly delay the survival of HP-tumour-bearing mice compared with FTn-Dox, H_2E-FTn-Dox and HSA-FTn-Dox (Fig. 6c). These results revealed that improving the vascular permeability properties of nanoparticles in LP tumours positively correlated with therapeutic outcomes, but had no significant effect on HP tumour penetration due to these tumours already possessing a high level of passive extravasation.

Conclusions

In this study, we created a ML-based single-vessel quantitative analysis method that was capable of high-throughput assessment of individual blood vessel features. By collecting thousands of vessel sections, this approach enabled correct quantitative characterization of intratumoural heterogeneity associated with the vascular permeability of nanoparticles. Based on the quantitative data, we manually classified permeable tumours into two categories (HP and LP) and permeable vessels into three categories (HP, MP and LP). This classification of permeability will undoubtedly provide valuable information for developing personalized therapeutic strategies for tumours. For example, our data demonstrated that improving active transendothelial transport was not a necessity for HP tumours, but was essential for efficient delivery in LP tumours. Additionally, we demonstrated that the approach facilitated understanding heterogeneous permeability mechanisms of blood vessels to accelerate the development of strategies to modulate vascular permeability. Future studies are also needed to explore the link between animal tumour models and clinical cases, using the single-vessel analysis method. Going forward, we anticipate that the single-vessel analysis method will be particularly useful for the development of highly permeable anticancer nanomedicines, and of value in the screening of inducers/inhibitors to modulate vascular permeability.

Our results demonstrated that vascular permeability was highly heterogeneous among different tumour types and different blood vessels. These data revealed that blood vessel features were essential determinants of nanoparticle permeability through the endothelium. However, our studies also support the view that the vascular permeability of nanoparticles can be modulated by rational design, especially for achieving active transendothelial permeability in LP tumours. In this regard, we developed a transcytosis-enhanced strategy by boosting

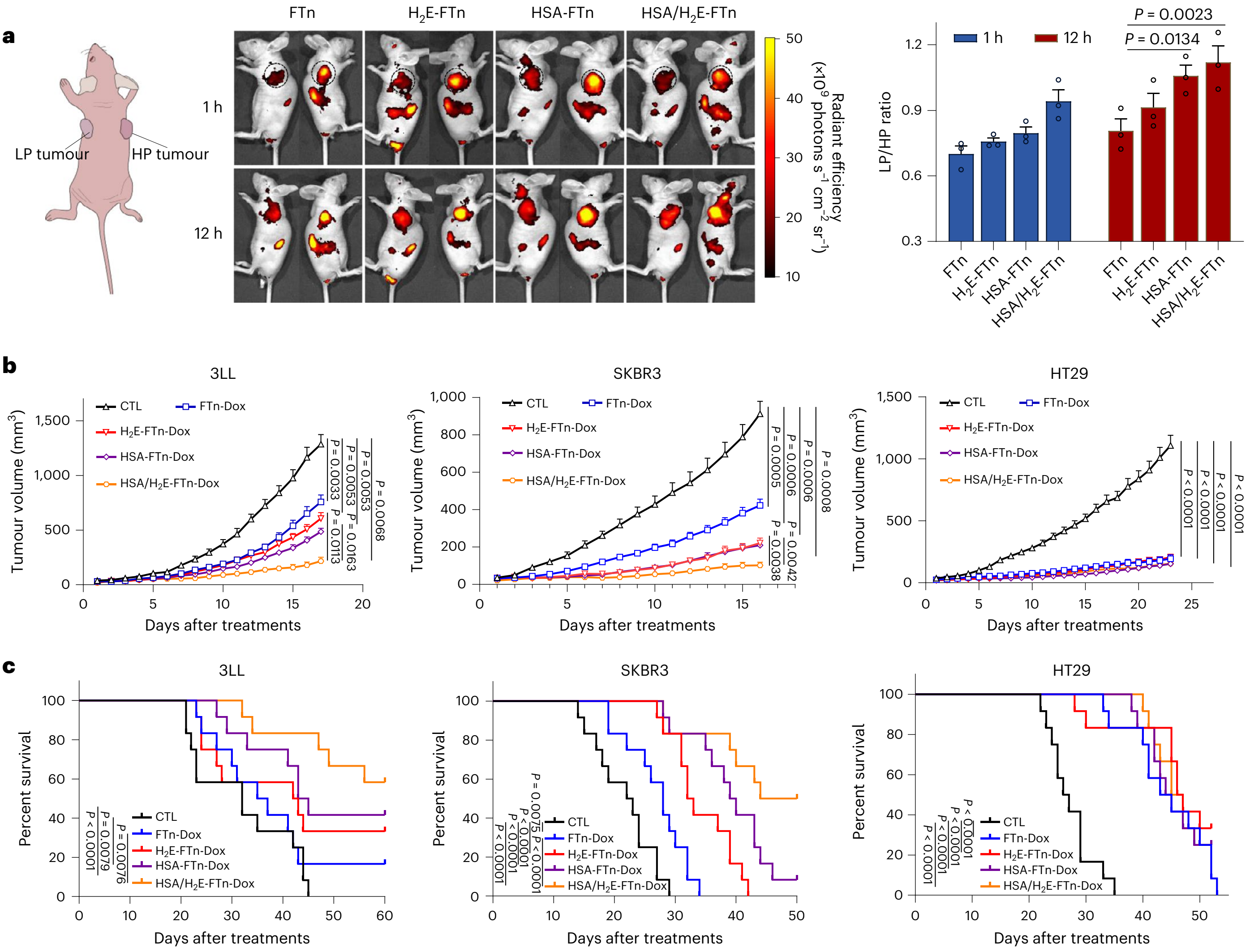

Fig. 6 | In vivo anticancer ability of different FTn formulations. a, In vivo fluorescent imaging and quantitative analysis of the distribution of FTn and its variants in mice bearing both LP tumours and HP tumours following intravenous injection for 1 and 12 h. The quantitative analysis was performed by determining the signal intensity of the LP tumour/HP tumour ratio in the same mouse. *n* = 3 mice per group. Tumours are indicated by black dashed circles. **b**, Tumour growth curves of different groups of various tumour-bearing mice after administration of the indicated treatments. *n* = 12 mice per group. **c**, Kaplan–Meier survival curve of the different tumour-bearing mice following different treatments. *n* = 12 mice per group. Data are presented as mean ± s.e.m. and statistical analysis was performed by one-way ANOVA with Tukey's post hoc test for comparison. The differences in the survival were analysed using the log-rank test.

the Golgi-dependent exocytosis pathway. Protein nanoparticles were designed with integrated lysosome-escaping motifs with HSA-binding motifs, with the aim of achieving a synergistic effect to reduce lysosome degradation by accelerating Golgi exocytosis. The evidence revealed that elevated exocytosis of nanoparticles from endothelial cells would be an ideal design principle for improving transendothelial transport, and this was especially important in achieving tumour penetration and drug delivery to LP tumours. Based on our mechanistic studies, several potential aspects are recommended to boost the vascular permeability of nanoparticles in LP tumours: (1) improve the blood circulation time of nanoparticles to increase the chance of capture and uptake by endothelial cells (that is, pinocytosis); (2) actively strengthen nanoparticle–endothelial cell interactions (for example, non-specific adsorption, receptor–ligand functionalization) to amplify cell uptake; (3) accelerate transcytosis of nanoparticles in endothelial cells (for example, boost exocytosis, minimize nanoparticle degradation); and (4) selectively improve the passive penetration capabilities of tumour blood vessels (for example, vasodilation).

Online content

Any methods, additional references, Nature Portfolio reporting summaries, source data, extended data, supplementary information, acknowledgements, peer review information; details of author contributions and competing interests; and statements of data and code availability are available at https://doi.org/10.1038/s41565-023-01323-4.

References

1. Jain, R. K. & Stylianopoulos, T. Delivering nanomedicine to solid tumors. *Nat. Rev. Clin. Oncol.* **7**, 653–664 (2010).
2. Blanco, E., Shen, H. & Ferrari, M. Principles of nanoparticle design for overcoming biological barriers to drug delivery. *Nat. Biotechnol.* **33**, 941–951 (2015).
3. Huang, X. et al. Hypoxia-tropic protein nanocages for modulation of tumor- and chemotherapy-associated hypoxia. *ACS Nano* **13**, 236–247 (2019).
4. Dvorak, A. M. et al. The vesiculo-vacuolar organelle (VVO): a distinct endothelial cell structure that provides a transcellular

pathway for macromolecular extravasation. *J. Leukoc. Biol.* **59**, 100–115 (1996).

5. Dvorak, A. M. & Feng, D. The vesiculo-vacuolar organelle (VVO). A new endothelial cell permeability organelle. *J. Histochem. Cytochem.* **49**, 419–432 (2001).
6. Claesson-Welsh, L. Vascular permeability—the essentials. *Ups. J. Med Sci.* **120**, 135–143 (2015).
7. Matsumura, Y. & Maeda, H. A new concept for macromolecular therapeutics in cancer chemotherapy: mechanism of tumoritropic accumulation of proteins and the antitumor agent smancs. *Cancer Res.* **46**, 6387–6392 (1986).
8. Sindhwani, S. et al. The entry of nanoparticles into solid tumours. *Nat. Mater.* **19**, 566–575 (2020).
9. Butler, K. T., Davies, D. W., Cartwright, H., Isayev, O. & Walsh, A. Machine learning for molecular and materials science. *Nature* **559**, 547–555 (2018).
10. Moen, E. et al. Deep learning for cellular image analysis. *Nat. Methods* **16**, 1233–1246 (2019).
11. Greenwald, N. F. et al. Whole-cell segmentation of tissue images with human-level performance using large-scale data annotation and deep learning. *Nat. Biotechnol.* **40**, 555–565 (2022).
12. Wei, Y. et al. Prediction and design of nanozymes using explainable machine learning. *Adv. Mater.* **34**, e2201736 (2022).
13. Lin, X. et al. Chimeric ferritin nanocages for multiple function loading and multimodal imaging. *Nano Lett.* **11**, 814–819 (2011).
14. Fan, K. et al. Magnetoferritin nanoparticles for targeting and visualizing tumour tissues. *Nat. Nanotechnol.* **7**, 459–464 (2012).
15. Litjens, G. et al. A survey on deep learning in medical image analysis. *Med. Image Anal.* **42**, 60–88 (2017).
16. Caicedo, J. C. et al. Data-analysis strategies for image-based cell profiling. *Nat. Methods* **14**, 849–863 (2017).
17. Falk, T. et al. U-Net: deep learning for cell counting, detection, and morphometry. *Nat. Methods* **16**, 67–70 (2019).
18. Todorov, M. I. et al. Machine learning analysis of whole mouse brain vasculature. *Nat. Methods* **17**, 442–449 (2020).
19. Zhang, Y. et al. Biomimetic design of mitochondria-targeted hybrid nanozymes as superoxide scavengers. *Adv. Mater.* **33**, e2006570 (2021).
20. Nagy, J. A., Chang, S. H., Shih, S. C., Dvorak, A. M. & Dvorak, H. F. Heterogeneity of the tumor vasculature. *Semin Thromb. Hemost.* **36**, 321–331 (2010).
21. Feng, D., Nagy, J. A., Dvorak, A. M. & Dvorak, H. F. Different pathways of macromolecule extravasation from hyperpermeable tumor vessels. *Microvasc. Res.* **59**, 24–37 (2000).
22. Bonam, S. R., Wang, F. & Muller, S. Lysosomes as a therapeutic target. *Nat. Rev. Drug Discov.* **18**, 923–948 (2019).
23. Rennick, J. J., Johnston, A. P. R. & Parton, R. G. Key principles and methods for studying the endocytosis of biological and nanoparticle therapeutics. *Nat. Nanotechnol.* **16**, 266–276 (2021).
24. Tai, W., Li, J., Corey, E. & Gao, X. A ribonucleoprotein octamer for targeted siRNA delivery. *Nat. Biomed. Eng.* **2**, 326–337 (2018).
25. Bern, M. et al. An engineered human albumin enhances half-life and transmucosal delivery when fused to protein-based biologics. *Sci. Transl. Med.* **12**, eabb0580 (2020).
26. Yokota, S. & Fahimi, H. D. Immunocytochemical localization of albumin in the secretory apparatus of rat liver parenchymal cells. *Proc. Natl Acad. Sci. USA* **78**, 4970–4974 (1981).
27. Shroyer, K. R. & Nakane, P. K. Immunohistochemical localization of albumin and in situ hybridization of albumin mRNA. *Cell Biochem. Funct.* **5**, 195–210 (1987).
28. Pelletier, L., Jokitalo, E. & Warren, G. The effect of Golgi depletion on exocytic transport. *Nat. Cell Biol.* **2**, 840–846 (2000).
29. De Matteis, M. A. & Luini, A. Exiting the Golgi complex. *Nat. Rev. Mol. Cell Biol.* **9**, 273–284 (2008).
30. Jiang, B. et al. A natural drug entry channel in the ferritin nanocage. *Nano Today* **35**, 100948 (2020).

Methods

FTn and its variants

FTn were prepared and purified according to our previously reported procedures[31,32]. H_2E-FTn and ABD-FTn were obtained by genetically incorporating an H_2E repeat (HHEHHEHHEHHEHHEHHEHHEHHEHHE) and ABD (albumin-binding domain, LAEAKVLANR ELDKYGVSDFYKRLINKAKTVEGVEALKLHILAALP) into the human ferritin heavy-chain 1 (FTH1) gene, respectively. For H_2E-FTn, the inserted H_2E-repeat gene was directly ligated to pET-21a(+) plasmid into which the ferritin heavy-chain gene had been inserted. To incorporate ABD into FTn, FTH1 and ABD-FTH1 genes were inserted into the double *cis*–*trans* pCDFDuet-1 plasmid. For ABD/H_2E-FTn, H_2E-FTH1 and ABD-FTH1 genes were ligated to double *cis*–*trans* pCDFDuet-1 plasmid, which self-assembled into H_2E-ABD-FTn in the subsequent expression because FTn is composed of 24 subunits. The obtained plasmids were transfected into BL21 *Escherichia coli*. The expression and purification of H_2E-FTn, ABD-FTn and H_2E-ABD-FTn followed the procedures used of FTn, as described above. For HSA binding, 10 molar equivalents of HSA (MB1866, Sigma) were reacted with ABD-FTn or ABD/H_2E-FTn at 4 °C overnight. The resulting mixture was susequently further purified with a Superose 6 increase 10/300 GL column to obtain HSA-FTn and HSA/H_2E-FTn, respectively. The concentration of FTn and FTn variants was measured with a bicinchoninic acid protein assay kit (PC0020-500, Solarbio). The morphology of FTn and FTn variants was characterized by TEM (H7600, Hitachi) following negative staining with 1% uranyl acetate or 2% phosphotungstic acid. The molecular weights and sizes of protein nanocages were determined by SDS–PAGE and size-exclusion chromatography. The zeta potentials and hydrodynamic diameters of FTn and FTn variants were measured using a Zetasizer Nano ZE (Malvern Instruments). FTn protein structure analysis was performed using PyMOL v.2.3.2 based on PDB ID 3AJO. The sequences encoding FTn, H_2E-FTn and ABD-FTn are available in Supplementary Table 4.

Labelling and Dox loading of FTn and its variants

For labelling of fluorescence dyes, FTn and FTn variants were reacted with 30 molar equivalents of Cy5-NHS ester or Cy5.5-NHS ester (Lumiprobe) at 4 °C for 12 h in PBS solution (pH 8.0), and then the mixture was purified with a PD-10 desalting column (GE Healthcare).

FTn possess a natural drug entry channel that exists on the shell, which facilitates the direct loading of small molecular drugs into the core. Dox (23214-92-8, Meryer) was loaded into FTn and its variants according to a previously reported method[30]. Briefly, 8 mg FTn or FTn variants were reacted with 3 mg Dox at 60 °C for 4 h in 20 mM Tris–HCl buffer (pH 8.0), and then centrifuged at 8,050 *g* for 10 min to separate the supernatant; the mixture was then purified with a PD-10 desalting column (GE Healthcare) to remove free Dox. The loaded Dox in each nanocage was calculated following a previous method[30].

Tumour models

All animals were handled in accordance with the policies and guidelines of the Animal Ethics Committee of Nankai University. A total of 32 tumour models were successfully constructed by grafting various tumour cells into different mouse species. The established tumour models were classified into three types: subcutaneous tumours (named by the cell lines), orthotopic tumours (that is, cell line-O) and mouse-tumour-cell-bearing nude mice (that is, cell line-N). The subcutaneous tumours were obtained by subcutaneously grafting tumour cells into the right shoulder of the mice. Mouse-derived tumour cells were allografted into C57BL/6 or BALB/c mice, and human-derived tumour cells were xenografted into Balb/c-nude mice. For the orthotopic breast cancer model, 4T1 cells were inoculated into the right inguinal fifth mammary fat pad of BALB/c mice. The orthotopic pancreatic tumour model was established by inoculation of Panc02 cells into the pancreas of C57BL/6 mice. The tumour growth was monitored every day, and tumour volume was calculated as (tumour length) × (tumour width)^2/2. Detailed information on cell lines, cell culture conditions, mouse and tumour models are listed in Supplementary Table 5.

Tumour tissue images

Mice bearing subcutaneous tumours were administered Cy5-labelled FTn (30 mg per kg (body weight)) by tail vein injection when tumours had grown to 300–400 mm^3 unless otherwise specified. For the orthotopic tumour model, tumour-bearing mice were intravenously injected with Cy5-labelled FTn (30 mg per kg (body weight)) 10 days after implanting tumour cells. Thirty minutes after administering the FTn, the mice were killed, and the tumours were harvested and embedded into optimal cutting temperature compound (OCT 4583, Sakura). Next, cryosections of tumour tissues were prepared (7 μm thickness) and immunostained with PE-anti-CD31 antibody (102508, BioLegend). To minimize the effect of spatial distribution on vascular permeability, the resulting cryosections of each tumour type contained the anterior, middle and posterior segments from three or four tumours. Following staining with 4,6-diamidino-2-phenylindole (DAPI; 0100-20, Southern Biotech), the slices were imaged by confocal microscopy (Zeiss LM710) with excitation/emission wavelengths of 405/461 nm (DAPI for nucleus), 565/578 nm (CD31 for blood vessel) and 633/670 nm (Cy5-labelled FTn), respectively. The image acquisition parameters for confocal microscopy were kept constant in different cryosections of various tumours, which is especially important for acquiring the signal from Cy5-labelled FTn. Because of the three-dimensional pattern of blood vessels in tumour tissue, at least 1,000 blood vessels were acquired and analysed for each tumour type to minimize the potential random information yielded by two-dimensional images. For the sequential sections, different tumour tissues (3LL, K180, HT29) were prepared for cryosection. A series of cryosections (7 μm thickness) were obtained. Immunostaining and image acquisition were performed following the above procedures.

For the Zombie model study, the Zombie mice were prepared as described elsewhere with some modifications[8]. Briefly, a flat-bottomed needle was inserted into the left ventricle and 20 ml of PBS solution containing 10 U ml^{-1} heparin sodium was perfused at a constant flow rate of 5 ml min^{-1} using a peristaltic pump. Next, 30 ml of 4% paraformaldehyde solution was perfused at the same flow rate and incubated for 30 min to fix the vascular system of the whole mouse. After removing the fixative, the solution containing Cy5-labelled FTn was added and circulated for 30 min. The tumours were subsequently harvested from the Zombie mice and the images containing blood vessels and FTn penetration were acquired as described above.

Image segmentation and single-vessel analysis

The source code can be accessed at https://github.com/balabilibili24/Confocal_images_analysis.git. All code is evaluated under Python 3.10.4 (https://www.python.org), unless otherwise stated.

Preprocessing. The raw images acquired from confocal microscopy were first preprocessed using Zen 3.1 software. The fluorescence intensities of blood vessels and FTn were adjusted to guarantee the image was clearly visible and all images from various tumour types were obtained at constant setting modes. Next, noise and artifacts were removed from the images by Gaussian smoothing processing with the fixed parameters. Finally, the images were exported for further analysis following adjustment of the image size to 1,024 × 1,024 pixels (physical dimension, 708.49 μm × 708.49 μm), which was utilized in the following procedures including training, annotation and feature extraction.

Model training. The classic U-net model has an end-to-end deep-learning network, which is typically used in biomedical image segmentation[33]. Using U-net as a basic framework, we developed two models, one to segment blood vessels and the other to segment FTn penetration. The two models are capable of independently segmenting images from two channels (that is, vessel and FTn penetration) but each vessel and its corresponding penetration were kept interconnected. For model training, 102 representative images were extracted from 32 tumour types; these comprised 70 images for model training and validation, and 32 images for model testing of each tumour type. The boundary of each vessel or the corresponding FTn penetration in the images were then manually annotated. To better quantify the vascular permeability, two kinds of images were excluded from the annotation: images containing the vessel signal but without that of the corresponding FTn; and similarly, where FTn penetration was observed but there were no corresponding vessels. A total of 70 annotated images were randomly divided into an 80% training dataset and a 20% validating dataset. A separate testing set with 32 additional images was used to monitor the segmentation performances of the model in terms of the Dice similarity coefficient. Next, the segmentation models are trained using backpropagation, and the hyperparameters of the model were selected by hyperparameter optimization. During the training process, Adam optimization with a batch size of 4 and an initial learning rate of 0.05 was adopted. Additionally, the maximum epoch number was set to 100. Data augmentation was performed to extend our samples and reduce the overfitting by flip, rotation and transpose, etc. All processes of segmentation model building and evaluation were implemented using the Pytorch v.1.5 deep-learning library on a machine with an NVIDIA RTX3090 graphics processing unit.

Interannotator experiment for segmentation. To reduce bias, three independent researchers annotated the images to determine the employed gold-standard labels. Before doing so, a general rule was followed for image annotation. Briefly, the outer contour of each vessel was manually annotated as the vessel channel, and the FTn penetration boundaries were annotated to determine FTn penetration regions. After annotation, the channel masks with only one of either FTn penetration or blood vessels were removed. Subsequently, the gold-standard labels were determined. The first researcher who imaged the data was responsible for randomly selecting 102 representative images from 1,802 confocal images obtained from 32 tumours. Two different researchers annotated the images independently and assessed the accuracy among different annotations using the Dice similarity coefficient. For all annotated images, the Dice scores among different annotations (that is, gold-standard labels) were defined as at least 0.85 (for an FTn penetration channel) or 0.95 (for a vessel channel), otherwise they were reannotated by the first researcher. Next, we performed an interannotator analysis to compare the nano-ISML segmentation with human-level annotations. The testing set (that is, 32 images) was manually annotated again by a fourth researcher. Afterwards, the accuracy between the annotations of the fourth researcher and the gold-standard labels was compared; the scores are listed in Supplementary Table 1.

Feature quantitative analysis. All confocal images obtained from various tumours were automatically segmented using the two U-net segmentation models established above. Subsequently, four basic features were extracted, including the total FTn coverage area for each vessel (A_{magenta}), the coverage area of each vessel (A_{green}), the total Cy5 fluorescence intensity for each vessel (F_{magenta}) and the Cy5 fluorescence intensity in each vessel and its lumen (I_{magenta}). Based on the four indices, nine important parameters of the images, including blood vessels, FTn penetration and the interface between vessel and FTn penetration (vessel-FTn), were automatically extracted for quantitative analysis by the models. Specifically, the extracted features of blood vessels contained vessel density (VD, vessel number per mm^2 tumour tissue), vessel area ($\mathrm{VA} = A_{\mathrm{green}}$, coverage area for each vessel) and total VA% (the percentage of total VA in total tumour tissue area for each image). The FTn penetration features included penetration area ($\mathrm{PA} = A_{\mathrm{magenta}}$, coverage area of FTn penetration for each vessel), total PA% (the percentage of total PA in total tumour tissue area for each image) and FTn penetration amount (FA, penetration amount of FTn for each vessel, $\mathrm{FA} = \mathrm{PA} \times F_{\mathrm{magenta}} - \mathrm{VA} \times I_{\mathrm{magenta}}$). For quantitative analysis of the penetration ability of individual vessels, the interface between the vessel and the corresponding FTn penetration consisted of the relative penetration area (RA, relative FTn penetration area for each vessel, $\mathrm{RA} = A_{\mathrm{magenta}} - A_{\mathrm{green}}$), penetration area ratio (PR, FTn penetration area ratio for each vessel, $\mathrm{PR} = A_{\mathrm{magenta}}/A_{\mathrm{green}}$) and vascular permeability (VP, FTn penetration ability for each vessel, $\mathrm{VP} = \mathrm{FA}/(A_{\mathrm{magenta}} \times F_{\mathrm{magenta}})$). The manual setting parameters and their formulae are listed in Supplementary Table 2. Afterwards, the above nine indices were quantitatively analysed to determine the features of vessel, penetration and permeability. Details of the extracted indices are shown in Supplementary Table 3. Finally, we compared the correlation between the nano-ISML extracted features and our manual gold-standard labels.

Vascular penetration mechanism

To visualize FTn penetration across tumour blood vessels with TEM, iron oxide nanoparticles were in situ incorporated into the FTn cavity. FTn-IO were prepared using our previously reported method[19]. FTn-IO (equivalent FTn, 250 mg per kg (body weight)) was administered via tail vein to 3LL tumour-bearing mice and to HT29 tumour-bearing mice. After 30 min, the tumour tissues were harvested, fixed and processed according to standard procedures for the preparation of biospecimens for TEM. The resulting samples were observed by TEM and the vascular penetration mechanisms were evaluated according to the distribution of observed FTn-IO. To explore the capture–uptake mechanisms, 32 typical vessels from 3LL tumours were observed and quantified by counting FTn-IO numbers under TEM. To determine vesicle sizes, the active or inactive vessels with typical features in 3LL tumours were analysed. To further verify the mechanism of FTn penetration through tumour vessels, we injected 200 µl of 50 mM EIPA (HY-101840, MCE), an inhibitor of pinocytosis, intratumorally into 3LL tumours. After 30 min, Cy5-labelled FTn was injected intravenously into tumour-bearing mice, and the vascular penetration was further analysed by nano-ISML.

In vivo near-infrared tumour imaging

To understand the in vivo dynamic behaviours of FTn, tumour-bearing BALB/c-Nude mice were intravenously injected with Cy5.5-labelled FTn (30 mg per kg (body weight)). Subsequently, tumour accumulation profiles were monitored on the front flank tumours of three mice using a Maestro all-optical imaging system at predetermined time points (10, 30, 60 and 180 min). Near-infrared fluorescence images of tumours were quantified by measuring near-infrared fluorescence intensity at the region of interest using the Maestro all-optical imaging system and accompanying software.

To compare tumour accumulation of LP tumours and HP tumours, Cy5.5-labelled FTn and its variants (equal Cy5.5 for different particles) were administered into SKBR3-bearing mice (left shoulder) and HT29-bearing mice (right shoulder) via the tail vein. At specific time points postinjection (1 and 12 h), the mice (n = 3 per group) were imaged by an IVIS Spectrum imaging system (IVIS Lumina II Xenogen, Caliper Life Sciences). The accumulation of FTn in tumours was semiquantitatively analysed with Living Image 2.50 software.

Subcellular localization

HUVECs were seeded on sterile coverslips and cultured overnight. The medium was replaced with fresh medium and Cy5-labelled FTn or FTn variants (20 µgml) were added to incubate for 2 h. For co-localization with lysosomes, the HUVECs were washed with PBS buffer and continued to incubate for additional time points in fresh medium (2, 4, 6 and 8 h). The cells were stained with LysoTracker Red (100 nM, Thermo Fisher Scientific) and Hoechst 33342 (20 nM, Thermo Fisher Scientific) at 37 °C for 15 min for co-localization with lysosomes. For co-localization with Golgi, the HUVECs treated with Cy5-labelled FTn or FTn variants were washed with PBS buffer and incubation continued for 4 h. The HUVECs were immunostained using anti-GALNT2 antibody (ab262868, Abcam) following a standard procedure. To study exocytosis of HUVECs, the co-localization of FTn and FTn variants with cell membrane was observed. Typically, the HUVECs treated with Cy5-labelled FTn or FTn variants were washed with PBS buffer and culture continued for an additional 6 h. The cells were stained with DiI (10 μM, Thermo Fisher Scientific) and Hoechst 33342 at 37 °C for 15 min. After the above staining, the subcellular localization (that is, lysosome, Golgi and cell membrane) of FTn and FTn variants were observed by Zeiss LM710 confocal microscopy excitation/emission wavelengths of 405/461 nm for nucleus, 565/578 nm for lysosome, Golgi or cell membrane, and 633/670 nm for FTn and FTn variants. The co-localization of FTn and FTn variants with subcellular organelles was quantitatively evaluated by determining the Pearson's coefficients. A Pearson correlation coefficient (P) between magenta signals and green signals was calculated according to the following formula:

$$P = \frac{\sum\left(M_i - \overline{M}\right) \times \left(G_i - \overline{G}\right)}{\sqrt{\sum\left(M_i - \overline{M}\right)^2 \times \sum\left(G_i - \overline{G}\right)^2}}$$

where $\overline{M}$ and $\overline{G}$ are the pixel-averaged intensities of the magenta signals and green signals, and M_i and G_i are the intensities of the magenta and green signals of pixel i in the images, respectively.

Transcytosis

To study the transcytosis of FTn and FTn variants, the HUVECs were first plated on sterile coverslips in cell culture dishes. FITC-labelled FTn and Cy5-labelled FTn variants (50 μg ml^{-1}) were simultaneously added to the HUVECs for 4 h incubation. The HUVECs were washed with PBS buffer at least three times before subsequent co-culture with coverslips plated with untreated tumour cells. The two cell-seeded coverslips were placed in an adjacent configuration within a culture dish containing fresh medium and incubated for an additional 12 h. Finally, the cells on the different coverslips were harvested and separately analysed by flow cytometry. The FITC signal from tumour cells was used as a control group to determine the assay with similar conditions. The effect of FTn and its variants on transcytosis were determined by the Cy5 signal of the tumour cells.

Plasma pharmacokinetics of FTn and FTn variants

Cy5-labelled FTn and FTn variants were injected into C57BL/6 mice via the tail vein at a dose of approximately 30 mg per kg (body weight) (equivalent Cy5 for FTn and FTn variants). The blood samples were collected at specific time points (3, 6, 10, 20, 30, 60, 120, 240, 480, 720 and 1,240 min), and were then centrifuged at 1,800 *g* for 10 min to separate the plasma. The concentrations of the FTn and FTn variants in the plasma were determined by measuring the fluorescence intensity at 640/670 nm.

Cell viability of FTn and FTn variants

Cytotoxicity was measured by a standard methyl thiazolyl tetrazolium (MTT) assay. Briefly, the cells were seeded into 96-well plates (4×10^3 cells per well). After 24 h, FTn and FTn variants (0, 2.5, 5, 10, 20 μg ml^{-1}) were added to the cells. After another 48 h incubation, the viability was assessed using a standard MTT method, and the relative cell viability was determined.

Cellular uptake of Dox-loading FTn and FTn variants

SKBR3 tumour cells were plated on glass-bottomed dishes (MatTek) at a density of 5×10^3 cells cm^{-2} and were cultured for 24 h prior to use. The cells were incubated with FTn-Dox, H$_2$E-FTn-Dox, HSA-FTn-Dox or HSA/H$_2$E-FTn-Dox (at 10 μM Dox concentration) for 4 or 12 h). After washing with PBS, the cells were fixed with 4% paraformaldehyde for 15 min, followed by 1.5 μg ml^{-1} DAPI staining at room temperature. The images of cells were acquired with a Zeiss LM710 confocal microscope.

In vivo antitumour activity

For mouse-derived LP tumour models, female C57BL/6 mice were subcutaneously inoculated with 3LL cells (5×10^5 cells per mouse) into the right flank. After 1 week, the mice were randomly divided into four groups (n = 12 per group) and intravenously administered with PBS, FTn-Dox, H$_2$E-FTn-Dox, HSA-FTn-Dox and HSA/H$_2$E-FTn-Dox at 5 mg per kg (body weight) Dox-equivalent doses every 3 days. For the human-derived LP tumour model, female BALB/c-Nude mice were subcutaneously injected with SKBR3 cells (5×10^6 cells per mouse) in the right flank. After 2 weeks, the mice were randomly divided into four groups (n = 12 per group). The mice for each group were intravenously administered PBS, FTn-Dox, H$_2$E-FTn-Dox, HSA-FTn-Dox and HSA/H$_2$E-FTn-Dox at 5 mg per kg (body weight) Dox equivalent every 3 days. For the human-derived HP tumour model, female BALB/c-Nude mice were subcutaneously injected with HT29 cells (1×10^6 cells per mouse) in the right flank. After 2 weeks, the mice were randomly divided into four groups (n = 12 per group) and given multiple doses of PBS, FTn-Dox, H$_2$E-FTn-Dox, HSA-FTn-Dox and HSA/H$_2$E-FTn-Dox at 5 mg per kg (body weight) Dox-equivalent doses every 3 days by tail vein injection. For all the mice, the tumour size and body weight were measured every day. In parallel, survival of animals was monitored daily.

Statistical analysis

Statistical analysis was done using Python and GraphPad Prism 8.0. The statistical differences between two groups and among multiple groups were analysed using Student's *t*-test and one-way/two-way ANOVA, respectively. The differences in survival were analysed using the log-rank test. All the results are expressed as mean ± s.e.m.

Reporting summary

Further information on research design is available in the Nature Portfolio Reporting Summary linked to this article.

Data availability

The authors declare that data supporting the findings of this study are available within the article and its Supplementary Information. All relevant data can be made available upon reasonable request to the corresponding authors. Source data are provided with this paper.

Code availability

The source code of machine learning-based model can be accessed at https://github.com/balabilibili24/Confocal_images_analysis.git.

References

31. Huang, X. et al. Protein nanocages that penetrate airway mucus and tumor tissue. *Proc. Natl Acad. Sci. USA* **114**, E6595–E6602 (2017).
32. Liu, Q. et al. Modular assembly of tumor-penetrating and oligomeric nanozyme based on intrinsically self-assembling protein nanocages. *Adv. Mater.* **33**, e2103128 (2021).
33. Ronneberger, O., Fischer, P. & Brox, T. U-Net: convolutional networks for biomedical image segmentation. *Med. Image Comput. Comput. Assist. Interv.* **9351**, 234–241 (2015).

Acknowledgements

This work was supported by the National Natural Science Foundation of China 91959129 (X.H.), 32271448 (X.H.), 82072054 (J.Z.), 31870999 (X.H.), the National Key Research and Development Program of China 2022YFA1105100 (X.H.), Tianjin Synthetic Biotechnology Innovation

Capacity Improvement Project TSBICIP-KJGG-014-03 (X.H.) and the Nankai University Hundred Young Academic Leaders Program.

Author contributions

M.Z., J.Z. and X.H. conceived the idea, collected data, conducted data analysis and performed all the experiments. Z.L. assisted with the development of the U-net model. M.Z. and X.H extracted data information from U-net. Q.L., Z.G., Z.Z., T.Q., J.T. and R.Z. performed cryosections and immunostaining. A.C.M. provided guidance and edited the manuscript. D.K., J.T. and X.Y. helped to guide part of experiments. X.H. designed and supervised all studies and wrote the manuscript.

Competing interests

The authors declare no competing interests.

Additional information

Supplementary information The online version contains supplementary material available at https://doi.org/10.1038/s41565-023-01323-4.

Correspondence and requests for materials should be addressed to Jie Tian, Xiyun Yan or Xinglu Huang.

Peer review information *Nature Nanotechnology* thanks Bjoern Menze, Constantinos Mikelis and the other, anonymous, reviewer(s) for their contribution to the peer review of this work.

Reprints and permissions information is available at www.nature.com/reprints.

nature portfolio

Corresponding author(s): Xinglu Huang

Last updated by author(s): Dec 15, 2022

Reporting Summary

Nature Portfolio wishes to improve the reproducibility of the work that we publish. This form provides structure for consistency and transparency in reporting. For further information on Nature Portfolio policies, see our Editorial Policies and the Editorial Policy Checklist.

Statistics

For all statistical analyses, confirm that the following items are present in the figure legend, table legend, main text, or Methods section.

n/a	Confirmed	
☐	☒	The exact sample size (*n*) for each experimental group/condition, given as a discrete number and unit of measurement
☐	☒	A statement on whether measurements were taken from distinct samples or whether the same sample was measured repeatedly
☐	☒	The statistical test(s) used AND whether they are one- or two-sided *Only common tests should be described solely by name; describe more complex techniques in the Methods section.*
☐	☒	A description of all covariates tested
☒	☐	A description of any assumptions or corrections, such as tests of normality and adjustment for multiple comparisons
☐	☒	A full description of the statistical parameters including central tendency (e.g. means) or other basic estimates (e.g. regression coefficient) AND variation (e.g. standard deviation) or associated estimates of uncertainty (e.g. confidence intervals)
☐	☒	For null hypothesis testing, the test statistic (e.g. *F*, *t*, *r*) with confidence intervals, effect sizes, degrees of freedom and *P* value noted *Give P values as exact values whenever suitable.*
☒	☐	For Bayesian analysis, information on the choice of priors and Markov chain Monte Carlo settings
☒	☐	For hierarchical and complex designs, identification of the appropriate level for tests and full reporting of outcomes
☐	☒	Estimates of effect sizes (e.g. Cohen's *d*, Pearson's *r*), indicating how they were calculated

Our web collection on statistics for biologists contains articles on many of the points above.

Software and code

Policy information about availability of computer code

Data collection	Zetasizer Nano ZE (Version 7.12) was used to collect the zeta potential and DLS data; Image Lab (Version 6.0) was used for obtaining SDS-PAGE images; Unicorn (Version 6.1) was used to collect Size exclusion chromatography analysis data; Skanlt software (Version 6.0) was used to obtain the BCA assay and Cy5 fluorescence intensity assay; FBD CellQuest™ Pro Software was used to collect flow cytometry data; Zen (Version 3.1) was used for obtaining Confocal images; Nano-ISML was used to process confocal images and obtain segmented images. All code for model training and analysis can be accessed at https://github.com/balabilibili24/Confocal_images_analysis.
Data analysis	All statistical analyses were performed on Graphpad Prism 9.3.1; SnapGene (Version 4.3.6) was used for the analysis of plasmid sequence; Flowjo (Version 10.6.2) was used for the analysis of flow cytometry data; Living image software (Version 1.5) was used to analyse NIR fluorescence images; Image J (Version 1.47) was used to analyze the Pearson's colocalization coefficient in confocal images. All code for model training and analysis can be accessed at https://github.com/balabilibili24/Confocal_images_analysis.

For manuscripts utilizing custom algorithms or software that are central to the research but not yet described in published literature, software must be made available to editors and reviewers. We strongly encourage code deposition in a community repository (e.g. GitHub). See the Nature Portfolio guidelines for submitting code & software for further information.

Data

Policy information about availability of data

All manuscripts must include a data availability statement. This statement should provide the following information, where applicable:

- Accession codes, unique identifiers, or web links for publicly available datasets
- A description of any restrictions on data availability
- For clinical datasets or third party data, please ensure that the statement adheres to our policy

The authors declare that data supporting the findings of this study are available within the article and its supplementary Information. All relevant data and colour-blind friendly figures can be made available upon reasonable request to the corresponding authors.

Human research participants

Policy information about studies involving human research participants and Sex and Gender in Research.

Reporting on sex and gender	*Use the terms sex (biological attribute) and gender (shaped by social and cultural circumstances) carefully in order to avoid confusing both terms. Indicate if findings apply to only one sex or gender; describe whether sex and gender were considered in study design whether sex and/or gender was determined based on self-reporting or assigned and methods used. Provide in the source data disaggregated sex and gender data where this information has been collected, and consent has been obtained for sharing of individual-level data; provide overall numbers in this Reporting Summary. Please state if this information has not been collected. Report sex- and gender-based analyses where performed, justify reasons for lack of sex- and gender-based analysis.*
Population characteristics	*Describe the covariate-relevant population characteristics of the human research participants (e.g. age, genotypic information, past and current diagnosis and treatment categories). If you filled out the behavioural & social sciences study design questions and have nothing to add here, write "See above."*
Recruitment	*Describe how participants were recruited. Outline any potential self-selection bias or other biases that may be present and how these are likely to impact results.*
Ethics oversight	*Identify the organization(s) that approved the study protocol.*

Note that full information on the approval of the study protocol must also be provided in the manuscript.

Field-specific reporting

Please select the one below that is the best fit for your research. If you are not sure, read the appropriate sections before making your selection.

☒ Life sciences ☐ Behavioural & social sciences ☐ Ecological, evolutionary & environmental sciences

For a reference copy of the document with all sections, see nature.com/documents/nr-reporting-summary-flat.pdf

Life sciences study design

All studies must disclose on these points even when the disclosure is negative.

Sample size	The in vitro experiments in this manuscript were performed 3 times at least . A minimum of 3 independent repeats is performed to evaluate significance. For the tumour penetration analysis, we selected 32 different tumour models, and each tumour type includes 4-5 tumours. To determine the hidden features of the images, we collected and analysed sufficiently large numbers of vessels, with at least 1,000 vessels per tumour and a total of 67,530 vessels analysed in 32 tumours. The in vivo anti-tumour efficacy studies were performed with 12 mice per group for HT29 HP tumour model, 3LL LP tumour model and SKBR3 LP tumour model, per standard protocols and to minimize the number of animals under experiment. No statistical methods were used to pre-determine sample sizes. Details regarding sample size of all experiments are provided in the Methods section and figure legends.
Data exclusions	No data were excluded.
Replication	All experiments were repeated for at least three times and experimental findings were reproducible. All annotated images were annotated by three separate researchers for each image. Details of experimental replicates are given in the figure legends.
Randomization	The experimental groups were allocated randomly.

Blinding	Most of the time, data collection and analysis were not performed blind to the conditions of the experiments. But for tumour penetration analysis, the investigators were blinded to the tumour types.

Reporting for specific materials, systems and methods

We require information from authors about some types of materials, experimental systems and methods used in many studies. Here, indicate whether each material, system or method listed is relevant to your study. If you are not sure if a list item applies to your research, read the appropriate section before selecting a response.

Materials & experimental systems

n/a	Involved in the study	
☐	☒	Antibodies
☐	☒	Eukaryotic cell lines
☒	☐	Palaeontology and archaeology
☐	☒	Animals and other organisms
☒	☐	Clinical data
☒	☐	Dual use research of concern

Methods

n/a	Involved in the study	
☒	☐	ChIP-seq
☐	☒	Flow cytometry
☒	☐	MRI-based neuroimaging

Antibodies

Antibodies used	1.PE-anti-CD31 antibody (BioLegend, AB_314331) 2.anti-GALNT2 antibody (Abcam, ab262868)
Validation	All antibodies were verified by the supplier and each lot has been quality tested. All validation statements are available on the antibody websites, respectively. 1.PE-anti-CD31 antibody: https://www.biolegend.com/en-us/products/pe-anti-human-cd31-antibody-882?GroupID=BLG5721 2.anti-GALNT2 antibody: https://www.abcam.cn/galnt2-antibody-ab262868.html.

Eukaryotic cell lines

Policy information about cell lines and Sex and Gender in Research

Cell line source(s)	3LL, 4T1, A375, B16, CT26, DAN-G, Hep3B, HepG2, HT29, HT1080, HUVEC, MC38, MCF-7, MDA-MB-231, Miapaca-2, Panc02, PC3, SKBR3, SW-1990, U87 were purchased from the American Type Culture Collection (Manassas, USA). BGC-823, MX-1, SMMC-7721 were purchased from Qingqi Biotechnology Development CO., LTD. K180, MB49 were kindly given by Dr. Hongkai Zhang (Naikai University Tianjin 300071, China).
Authentication	Cell lines were not authenticated.
Mycoplasma contamination	The cell lines regularly tested for mycoplasma contamination, and no mycoplasma contamination was found.
Commonly misidentified lines (See ICLAC register)	No commonly misidentified cell lines are used in this study.

Animals and other research organisms

Policy information about studies involving animals; ARRIVE guidelines recommended for reporting animal research, and Sex and Gender in Research

Laboratory animals	Female BALB/c mice (4-5 weeks old), female C57BL/6 mice (4-5 weeks old), female BALB/c-Nude mice (4-5 weeks old) were purchased from SPF Biotechnology (Beijing, China).
Wild animals	The study did not involve wild animals.
Reporting on sex	*Indicate if findings apply to only one sex; describe whether sex was considered in study design, methods used for assigning sex. Provide data disaggregated for sex where this information has been collected in the source data as appropriate; provide overall numbers in this Reporting Summary. Please state if this information has not been collected. Report sex-based analyses where performed, justify reasons for lack of sex-based analysis.*
Field-collected samples	No field collected samples were involved in this study.
Ethics oversight	All animals were handled in accordance with the policies and guidelines of the Animal Ethics Committee of Nankai University.

Note that full information on the approval of the study protocol must also be provided in the manuscript.

Flow Cytometry

Plots

Confirm that:

☒ The axis labels state the marker and fluorochrome used (e.g. CD4-FITC).

☒ The axis scales are clearly visible. Include numbers along axes only for bottom left plot of group (a 'group' is an analysis of identical markers).

☒ All plots are contour plots with outliers or pseudocolor plots.

☒ A numerical value for number of cells or percentage (with statistics) is provided.

Methodology

Sample preparation	Cells were trypsinized, harvested and washed with PBS and then analysed with flow cytometer.
Instrument	The data were acquired using FACSCalibur™(Becton Dickinson, San Jose, USA)
Software	FlowJo software package (Flowjo V10.6.2)
Cell population abundance	Each experiment involved only one type of cell lines and no sorting was performed.
Gating strategy	For cellular uptake measurement, the gate was set to "viable" cells in FSC/SSC plot, and from those populations of live cells were gated.

☒ Tick this box to confirm that a figure exemplifying the gating strategy is provided in the Supplementary Information.